Rain Relations Inferred from Microphysical Data in TOGA COARE and Their Use to Test a Rain-Profiling Method from Radar Measurements at K_u-Band

VIRGINIE MARECAL, TAOUFIK TANI, PAUL AMAYENC, CLAUDE KLAPISZ, ESTELLE OBLIGIS, AND NICOLAS VILTARD

Centre d'Etudes des Environnements Terrestre et Planetaires, Velizy, France

(Manuscript received 2 December 1996, in final form 8 April 1997)

ABSTRACT

The first part of this paper is dedicated to establishing relations among rain-integrated parameters representative of west Pacific precipitation. This is achieved by using airborne microphysical data gathered within a rain event on 6 February 1993 during the Tropical Ocean and Global Atmosphere Coupled Ocean–Atmosphere Response Experiment (TOGA COARE). The relations between the rain rate R, the reflectivity factor Z, and the attenuation coefficient K are calculated for moderate to heavy precipitation at 13.8 GHz. They give twice as much attenuation for a given Z than the relations obtained for an exponential distribution with $N_0 = 8 \times 10^6$ m^{-4}. This effect is related to the large number of small size particles observed in TOGA COARE convective systems.

In the second part of the paper, these relations are used to check the reliability of a rain-profiling method applied to ARMAR (airborne radar-mapping radar) observations at 13.8 GHz in the same rain event. This method provides a bulk correction factor that can be interpreted primarily in terms of a change of the initial Z–K relation. Then, the algorithm provides modified Z–R and K–R relations while assuming a gamma or an exponential-shaped distribution for raindrops with a constant N_0. For the selected case study, the adjusted relations agree very well with those derived from the microphysical measurements. An exponential shape model with constant N_0 for the DSD is found to provide results that are consistent with the microphysical measurements. Moreover, the derived N_0 value is close to that inferred from the radar algorithm. The impact of modifying the initial rain relations in the radar algorithm on the rain-rate estimates is also discussed. The retrieved rain rates are not very sensitive to the choice of initial relations except for very high values. Finally, the results are found more representative of convective rain than stratiform precipitation.

1. Introduction

The general goal of the TOGA COARE (Tropical Ocean and Global Atmosphere Coupled Ocean–Atmosphere Response Experiment) campaign is to study the coupling between the atmosphere and the west Pacific ocean warm pool and to evaluate its effect on the global climate (Webster and Lukas 1992). Estimation of the rainfall associated with the observed convective systems represents an important aspect of the experiment. Rainfall-related parameters at different space–timescales were measured from rain gauges, airborne microphysical probes, shipborne or airborne radars, multichannel microwave radiometers, etc. Such data coupled with three-dimensional wind field observations from Doppler radars may be used for understanding basic processes in the formation and growth of the precipitation. Also, they may be employed to get relations between rain-related integrated parameters and to test radar algorithms for estimating rainfall, which are known to be sensitive to the variability of such relations. The present paper deals with this second aspect by using data from the airborne microphysical probes mounted aboard the Electra (NCAR) aircraft, and from the Airborne Rain-Mapping Radar (ARMAR) installed on board the DC8 (NASA) aircraft.

Rain relations vary for different climate regimes or rain types, according to changes in the characteristics of the raindrop size distributions. Battan (1973) clearly pointed out this variability by listing 69 Z–R relations (between the radar reflectivity factor Z and the rain rate R) available from various experimental works. Since 1973, this list has greatly increased. Drop size distribution (DSD) data provided by microphysical probe measurements aboard Electra during TOGA COARE are well suited to get rain relations ''tuned'' to convective rainy systems observed over the west Pacific ocean. The first objective of this paper is preparing a subsequent use in the exploitation of radar data.

ARMAR (Durden et al. 1994) is a simulator of the future Tropical Rainfall Measuring Mission (TRMM) radar (Simpson et al. 1988) at K_u band (13.8 GHz) with downward-looking geometry and cross-track scanning

Corresponding author address: Virginie Marecal, Centre d'études des Environnements Terrestre et Planétaires (CETP), 10-12 Avenue de l'Europe, 78140 Vélizy, France.
E-mail: Virginie.MARECAL@cetp.ipsl.fr

to provide detailed mapping of the precipitation while overflying rainy systems. At 13.8 GHz, path-integrated attenuation (PIA) due to rain affects the reflectivity measurements especially in intense rain cores. This leads to underestimation of the rain rate derived from a Z–R relation using the ''apparent'' reflectivity factor Z_m (uncorrected for PIA) instead of the true reflectivity factor, even if the Z–R relation is climatologically tuned. Numerous attenuation-compensating algorithms were proposed, and occasionally tested from airborne experiments, to get range-profiled rain rates (e.g., Meneghini and Nakamura 1990; Meneghini et al. 1989, Meneghini et al. 1992; Kozu et al. 1991; Marzoug and Amayenc 1994; Amayenc et al. 1996). Many of them, for single-frequency mode, were developed to prepare a future exploitation of the TRMM radar data. Comparing rain-rate retrievals from different range-profiling algorithms applied to ARMAR data and pointing out their sensitivities to various error sources is not our purpose. This will be examined in a future paper. Here, only the rain profiling method proposed by Amayenc and Tani (1995) is considered. This global adjustment method (or GA method) provides a bulk correction factor that can be interpreted in terms of a modification of the reference rain relations used in the algorithm. The TOGA COARE experiment provides a unique opportunity to check the reliability of such adjustment applied to ARMAR data by comparing with the rain relations derived from the DSD data gathered in the same rain system. This is the second objective of the paper.

The case selected for this study is a long-living mesoscale convective system sampled during coincident flights of the two aircraft. Section 2 describes the features of the rain system along with the used ARMAR and microphysical datasets. The principle and the main characteristics of the GA method are recalled in section 3. A large part of the paper (section 4) is devoted to the microphysical data analysis to get reliable rain relations at 13.8 GHz from the DSD measured by the Electra PMS-2D probes. This part includes sensitivity tests to the assumptions used in the data processing. The combined use of results from the GA method and the microphysical analysis to test the adjustment of rain relations is discussed in section 5. The impact of modifying the initial rain relations used in the algorithm on rain rate estimates is also pointed out. Conclusions are given in section 6.

2. Experiment and data characteristics

Observations were taken on 6 February 1993 over the Pacific Ocean within a mesoscale convective system oriented northwest–southeast and located near $-12°$N and 156°E, southwest of the warm pool, on the periphery of the tropical cyclone Oliver (about 700 km northeast of Oliver's eye). The system was slowly advected at 6 m s^{-1} toward east-southeast and elongated in a direction parallel to this propagation axis. Its horizontal extent was about 60 km in width and more than 200 km in length. A description of the kinematic and thermodynamic characteristics of the system can be found in Roux and Moine (1996). This observation was selected as one of the best cases of coincident samplings taken by the Electra 2D probes and the ARMAR on the DC8. Note that the two P3 (NOAA) aircraft were also involved in coincident flights for this case.

Figure 1 displays six reflectivity composites between 1630 and 2000 UTC, each being constructed from 35-min radar observations at 4-km altitude within rain from one P3 aircraft. The altitude of the 0°C isotherm was 4.7 km. The composites show the system and its time evolution. The small-scale structure within the rainband is composed of a series of convective cells evolving with time with a continuous process of creation/dissipation. At the mesoscale, however, the rainband lasted from 1630 to 2000 UTC with no major change in its global structure.

The DC8 flight altitude was 9.4 km. The radar, operating in pulse compression mode, had a range resolution of 60 m, and performed range-gated measurements with about 100 independent samples per instantaneous field of view. At 9.4-km range, the beam footprint size at nadir is close to 600 m, and the minimum detectable apparent reflectivity is about 9 dBZ. The high beam resolution likely prevents severe effects of nonuniform beam filling in the measurements. Polarization diversity and Doppler information were not used here; horizontally polarized signal only was considered (i.e., the electrical vector is parallel to the surface at any beam incidence). The radar beam operated cross-track scanning within a $\pm 20°$ angular interval every 2 s. Accounting for the aircraft flight speed (220 m s^{-1}), the sampling step for a given beam incidence in along-track direction is 440 m, slightly less than the beam footprint size. Two ''rain'' time sequences, S1 (1631:07–1643:45 UTC), and S2 (1802:04–1812:20 UTC), each one corresponding to about 150-km leg along the rainband, were considered. Reference measurements of surface echo outside rain, required to process the radar algorithm, were performed in ''clear air'' regions within a time sequence S3 (1757:15–1802:02 UTC) adjacent to rain data of sequence S2.

The microphysical data were collected within rain at 3.2-km altitude from 1630 to 2000 UTC while the Electra crossed over the rainband several times (see Fig. 2). Each DSD is obtained over a 6-s integration time corresponding to a trajectory length of about 0.7 km. Since the reflectivity and attenuation are more important for large raindrops than for small droplets, the data used are essentially those of the PMS-2DP probe, which samples particles with the diameter ranging from 0.2 to 6.4 mm every 0.2 mm (32 classes). The possible contribution of smaller droplets was also evaluated using data of the PMS-2DC probe, which samples particles with the diameter ranging from 25 to 800 μm every 25 μm (32 classes).

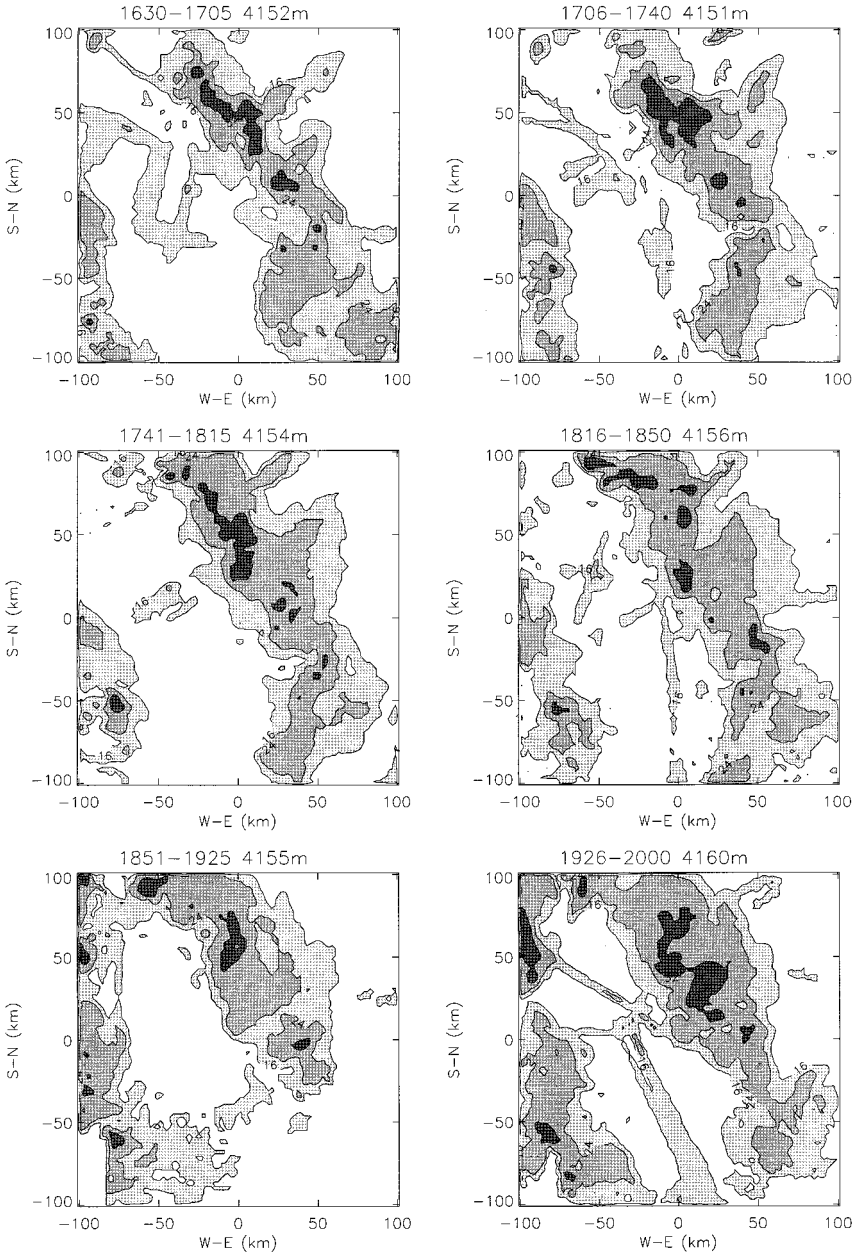

FIG. 1. Composites of reflectivity factor contours (in dB*Z*) between 1630 and 2000 UTC, calculated from the data of the lower fuselage radar mounted onboard the P3-N42RF aircraft (NOAA). The title of each composite gives the time interval (UTC) of the considered sequence and the mean altitude (m) of the aircraft. The southern part of the rainband does not appear in the fifth composite (1851–1925 UTC) because the aircraft trajectory is confined in the northern part of the domain.

The sampling volumes are much smaller for the airborne probes than for ARMAR. Therefore, to set relevant conditions of comparison between the two types of measurements, a large number of microphysical samples over a spatial extent comparable to that covered by the radar observations is required. The microphysical measurements used are those gathered between 1630 and 2000 UTC while the global structure of the system was rather steady. The stationarity hypothesis was tested by applying the microphysical analysis to data subsets taken over shorter time intervals (~1 h). The results are close to those obtained for the total period with, however, more scattering owing to the smaller number of data points involved in the analysis. Also, results of the radar algorithm for the sequences S1 and S2, which are about 90 min apart, are very similar (see section 5).

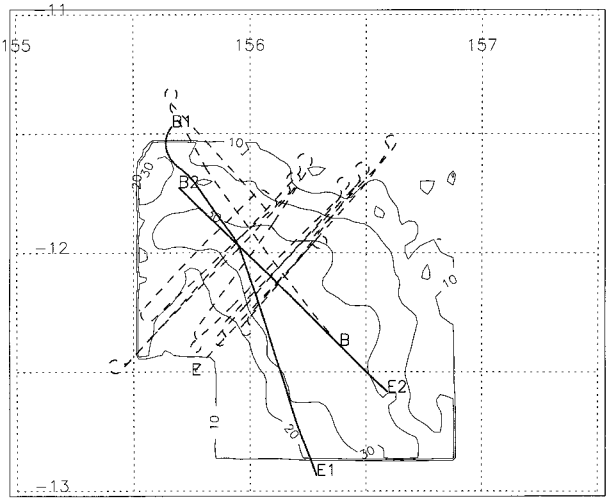

FIG. 2. Electra (bold dashed line) and DC8 trajectories (bold line) and major contours of the mean reflectivity factor field (dBZ) between 1630 and 2000 UTC derived from the data of the tail radars (9.4 GHz) mounted on board the Electra (NCAR), the P3-N42RF (NOAA), and the P3-N43RF (NOAA) aircraft. Numbers indicate east longitude and south latitude. Letter B (E) refers to the beginning (end) of every aircraft trajectory.

These points support the assumption that the system could be considered as globally stationary from the point of view of this study. Besides, ARMAR performed measurements over the whole rain layer while the microphysical probe data were collected at 3.2-km altitude only; this point is discussed in section 4e.

Figure 3 displays the vertical cross section of the ''apparent'' reflectivity factor measured versus range (from the radar) from nadir-pointing observations with ARMAR during sequence S2. To keep the figure easily readable, the picture is limited to the second half of sequence S2—that is, from 1807:30 to 1812:20 UTC. The strong echo near the 9.4-km range is the surface return. For convenience, it has been expressed in the same unit as rain reflectivity. The mirrored rain echoes, obtained after two reflections of the incident wave on the surface, appear at ranges greater than the surface range r_S, as if they were returned from below the surface. Figure 4 shows the total two-way PIA (expressed in decibels greater than 0) over the entire rain-layer depth, estimated from the surface reference technique (Meneghini et al. 1983) for the same time period as in Fig. 3. This PIA estimate, further used as a constraint in the radar algorithm (see section 3), was obtained by forming the ratio of surface return powers outside rain (measured

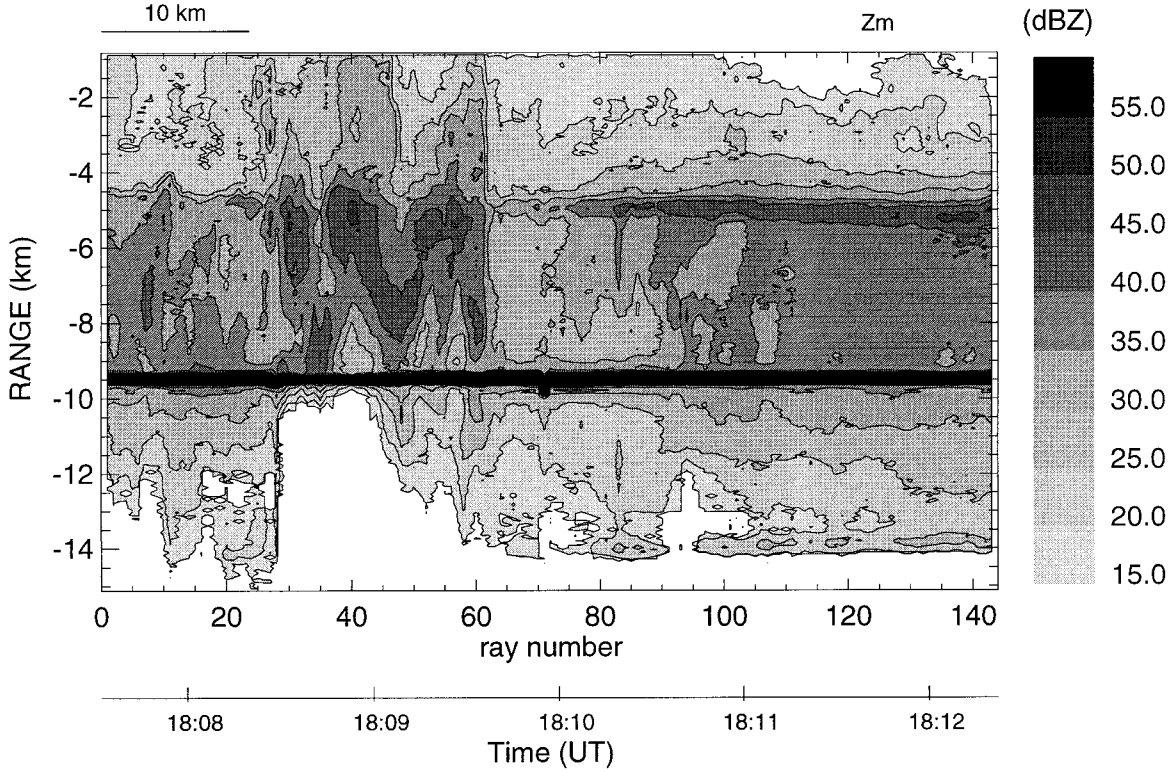

FIG. 3. ''Apparent'' reflectivity factor (dBZ) as a function of range from the radar, measured by ARMAR for nadir-pointing conditions during the second half of sequence S2 (from 1807:30 to 1812:20 UTC). The surface echo near the 9.4-km range is expressed in the same unit. The ray number on the abscissa corresponds to the successive observations at nadir, about every 2 s, during the cross-track scanning of the radar beam. The acquisition time is given on a separate axis at the bottom. The scale for the equivalent horizontal distance is indicated in the upper left of the panel.

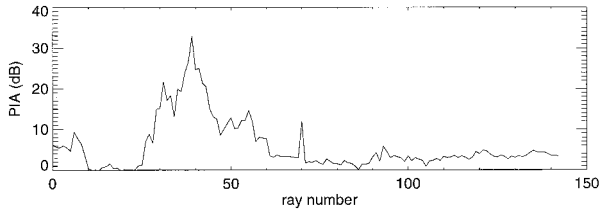

FIG. 4. Path-integrated attenuation (PIA) derived from surface echo measurements by ARMAR at vertical incidence for the same ray numbers and time frame as shown in Fig. 3.

during sequence S3) and below rain, while assuming that surface roughness was not affected by surface wind or by drop impact on ocean surface (Moore et al. 1979; Atlas 1994), and that the observed decrease in the surface return power was essentially due to attenuation by rain. The reference σ^0 value measured outside rain was 12.9 dB at nadir with a standard deviation of 0.35 dB, and -0.6 dB at 18° incidence with a standard deviation of 0.7 dB (Tani et al. 1995). In Fig. 3, it appears that between 1808:30 and 1809:30 UTC the radar encountered a convective zone characterized by the presence of an intense rain cell with reflectivity peak greater than 40 dB*Z* aloft. A severe attenuation effect, evidenced in Fig. 4 by an increase in the total PIA up to 33 dB, produces a decrease of apparent rain reflectivity toward the surface (near 1809 UTC), and a correlative decrease or even a disappearance of the mirrored echoes. Stratiform precipitation is identified on the right-hand side (1809:30–1812:20 UTC) by the presence of a bright band peaking at 5-km range from the radar or 4.4-km height. In the rain zone below, low attenuation, as seen in the PIA, does not affect the reflectivity field much. Note that the ''blip'' seen in the surface return in Fig. 3, as well as the spike in the PIA in Fig. 4 near ray number 70, are due to the fact that the aircraft overflies a small island. Hitting the land while assuming an ocean background leads to overestimation of the reference σ^0 and then to an artificial increase in the PIA.

3. The global adjustment method for rain-rate profiling

a. Formulation

The global adjustment method relies on minimizing the difference (over a set of measurements) between the surface–reference-derived attenuation and the Hitschfeld–Bordan-derived attenuation to get a correction factor as follows. Let us start from the class of range-profiling algorithms, correcting for the PIA, defined by Marzoug and Amayenc (1994). All these algorithms make use of a $Z = \alpha K^{\beta}$ relation in the radar equation for rain echoes to get first the K (or Z) profile versus range. Then, the rain-rate profile is obtained from the $K = aR^b$ (or $Z = eR^d$) relation. The set of three relations have to be self-consistent in the sense that each relation can be obtained by combining the other two. In every relation, it is assumed that the exponent is a known constant and that the multiplying coefficient is range-free but possibly adjustable. The general expression for K at range r is

$$K(r) = [Z_m(r)/\alpha]^{1/\beta}/[\{fA(r_0, r_s)\}^{1/\beta} + \gamma S(r, r_s)], \quad (1)$$

where $\gamma = 0.46/\beta$ and the term

$$S(r, r_s) = \int_r^{r_s} [Z_m(s)/a]^{1/\beta}\, ds \quad (2)$$

involves the apparent reflectivity factor $Zm(r)$. In the same equation, $A(r_0, r_S)$ is the total two-way PIA factor (between the rain top range r_0 and the surface range r_S), which may also be derived from integration of radar equation according to

$$A(r_0, r_s) = [1 - f^{-1/\beta}\gamma S(r_0, r_s)]^{\beta}, \quad (3)$$

where

$$f = \delta\alpha\delta C \quad (4)$$

is a correction factor including range-free scaling errors $\delta\alpha$ in the α coefficient of the Z–K relation and δC in the radar calibration constant C. Every error term $\delta\alpha$ (or δC) is a positive multiplying factor of the α (or C) value used initially; no correction of α and C implies $f = 1$.

The total PIA factor $A(r_0, r_S)$ may be evaluated from (3) while assuming $f = 1$, as in the well-known approach proposed by Hitschfeld and Bordan (1954), which processes rain echoes only. However, the presence of scaling errors ($f \neq 0$) may have significant impact on the results of the profiling algorithms. Meneghini and Nakamura (1990) and Iguchi and Meneghini (1994) proposed a ''local'' determination of f, referred to as α or C adjustment, by setting $A(r_0, r_S) = A_{\text{tm}}$, the total PIA factor ''measured'' from the attenuation of surface echo below rain. Note that, in their own notations, the correction factor ε identifies with $f^{-1/\beta}$ here. The local correction factor is derived from (3) as

$$f = [\gamma S\,(r_0, r_S)/(1 - A_{\text{tm}}^{1/\beta})]^{\beta} \quad (5)$$

for every considered path within the rain system. In the GA method of Amayenc and Tani (1995), a similar approach is used but on ''global'' basis by means of a least squares fit minimizing the rms deviation between $A_i(r_0, r_S)$ and $A_{\text{tm},i}$ over a set of N selected paths (with current index $i = 1, \ldots, N$) in the rain system. This is achieved by minimizing the functional

$$J = \sum_{i=1}^{N} [A_i^{1/\beta}(r_0, r_s) - A_{\text{tm},i}^{1/\beta}]^2, \quad (6)$$

which provides an ''adjusted'' bulk correction factor f_B given by

$$f_B = \left[\frac{\gamma \sum_{i=1}^{N} S_i^2(r_0, r_s)}{\sum_{i=1}^{N} (1 - A_{\mathrm{tm},i}^{1/\beta}) S_i} \right]^{\beta}. \quad (7)$$

b. Main characteristics

It was verified analytically as well as tested experimentally (see section 5) that f_B weakly depends on β, which is close to unity in (7). Using the local approach, results for f may be sensitive to local random errors in A_{tm}, especially for low PIA where $A_{\mathrm{tm}} \approx 1$. In practice, with real data, ''measured'' values of A_{tm} slightly in excess of 1, though nonphysical, are not uncommon. In such cases, use of (5) leads to a meaningless ''negative'' f estimate. In the global approach, this drawback may be overcome by ignoring A_{tm} values corresponding to a PIA below a prescribed low threshold (e.g., 1 dB) in the fitting process yielding f_B from (7). However, the dynamic range in the PIA factors over the selected N paths must be sufficiently large to get an accurate f_B estimate. An overall bias in A_{tm} resulting, for example, from an offset in the σ^0 value ''measured'' outside rain may also contaminate the f_B value; this has been checked from experimental data (see section 5). Finally, determining f_B is a way to point out a possible ''mean'' bias $\delta\alpha\delta C$ in the involved dataset while smoothing out random errors in ''local'' f values. Examining the goodness of the fits and the stability of f_B values obtained for different sets of N paths is required to assess the significance of the results.

In either the local or global approach, specifying α or C correction is not required to get the K profiles, which involve the $\delta\alpha\delta C$ product only. However, the type of correction must be further specified to get the Z or R profile since rain relations used for this purpose have to be modified (case of α adjustment) or not (case of C adjustment). In this sense, the adjustment is not unique. If the calibration error may be neglected ($\delta C \approx 1$), f_B may be interpreted mainly in terms of global α adjustment in Z–K relation. For Γ-shaped DSDs—where $N(D) = N_0 D^{\mu} \exp(-\lambda \mathrm{D})$—with a constant intercept parameter N_0, analytical considerations show that any power–law relation Y–aX^t between integrated rainfall parameters Y and X can be rewritten as $Y = gN_0^{(1-t)}X^t$, where g is constant (Ulbrich 1983; Marzoug and Amayenc 1994). Change of N_0 for a different value N_0^* implies change of a for a^* given by

$$a^* = a\delta a = a(N_0^*/N_0)^{(1-t)}. \quad (8)$$

Thus, any correction δa, associated with change of N_0 for N_0^*, can be used to infer the correlative correction $\delta a'$ of the a' coefficient of any other relation $Y' = a'X'^{t'}$ according to

$$\delta a' = \delta a^{(1-t')/(1-t)}, \quad (9)$$

provided that exponents (t, t') in the relations and the shape parameter μ of the DSD are assumed to be constant. Thus, using these hypotheses, any correction factor f_B interpreted in terms of $\delta\alpha$ correction in the $Z = \alpha K^{\beta}$ relation can also be used to infer an N_0 correction given by

$$N_0^*/N_0 = f_B^{1/(1-\beta)} \quad (10)$$

and the correlative corrections δa in the $K = aR^b$ relation and δe in the $Z = eR^d$ relation according to

$$\delta a = \delta\alpha(1 - b)/(1 - \beta) \quad (11)$$

$$\delta e = \delta\alpha(1 - d)/(1 - \beta). \quad (12)$$

This is, in essence, a degraded version of the N_0 adjustment method of Kozu and Nakamura (1991), which assumes that all coefficients in the rain relations follow a prescribed N_0 dependence, whereas here, only the multiplying parameter in each relation is adjusted.

In the following, the GA method is used to get experimental determination of f_B and to compare the adjusted rain relations to those derived from microphysical analysis. An important point to keep in mind is that the bulk correction factor must be regarded as being representative of the entire rain layer, as a consequence of assuming range-free parameters in all rain relations.

4. Analysis of microphysical data

a. Data processing

The major objective of the microphysical data analysis was to establish reliable relationships between the attenuation factor K, the rainfall rate R, and the reflectivity Z at 13.8 GHz. To set the most appropriate conditions for further comparison with radar results, several aspects in microphysical data processing were dictated by specific conditions encountered in radar measurements. They are discussed sequentially in the course of the paper.

The first step was to calculate the integral parameters K, Z, and R directly from each measured DSD by using the following definitions:

$$Z = \frac{\lambda^4 \times 10^{18}}{\pi^5 |\kappa|^2} \int_D N(D)\sigma_b(D)\, dD, \quad (13)$$

$$K = 4.343 \times 10^3 \int_D N(D)\sigma_a(D)\, dD, \quad (14)$$

and

$$R = 3.6 \times 10^6 x \frac{\pi}{6} \int_D N(D)_v(D) D^3\, dD, \quad (15)$$

where D is the drop diameter in m, $N(D)$ is the size distribution in m^{-4}, Z is in $\mathrm{mm}^6\ \mathrm{m}^{-3}$, K is in dB km^{-1}, and R is in mm h^{-1}.

In (13), Z is the ''equivalent'' reflectivity factor since the Rayleigh approximation is not valid over the whole raindrop size range at 13.8 GHz, $|\kappa|^2 = 0.93$ is a di-

mensionless coefficient related to the water refractive index, λ is the radar wavelength (m), and $v(D)$ is the terminal fall speed (m s^{-1}) of raindrops. For $v(D)$, the experimental values given by Gunn and Kinzer (1949) were used. There is no correction for change in air density with altitude included in the terminal fall speed calculation. This means that R is calculated as if the DSDs were measured with terminal fall speed arbitrarily taken at the surface level instead of the aircraft level. This is consistent with the radar algorithm processing where the involved R-dependent relationships are used with the same hypothesis.

In (13) and (14), $\sigma_b(D)$ and $\sigma_a(D)$ (m^2) represent the raindrop backscattering and extinction cross sections, respectively. They depend on the drop temperature and on the incident wave frequency and polarization. They can be computed using the Mie diffusion theory while assuming spherical raindrops. It is known, however, that a raindrop flattens when its size increases, owing to aerodynamical effects. Thus, we chose to consider raindrops as spheroids. It was assumed that their long axis is oriented horizontally according to the mean orientation of flattened raindrops observed in nature. Here, σ_b and σ_a were computed using the T matrix approach (Waterman 1965). Nadir-looking conditions fitting to ARMAR geometry was used. Depending on the raindrop temperature T_R, the refractive index was computed using the Ray (1972) formulation that is assumed to be a mean temperature representative of the rain layer. The mean air temperature measured by dropsondes in the rain layer was $T_A \sim 14$°C. Since T_R is generally lower than T_A, it is assumed that $T_R = 10$°C. Effects of temperature and incidence angle on the results are discussed in section 4e.

The Black and Hallet (1986) method was used to calculate the DSDs. The larger particles recorded by the 2DP probe provide a major contribution to K, Z, and R. On the other hand, the probability that the probe records a particle of very large size in a 6-s duration is very low. Nevertheless, isolated very large particles are present in the original DSDs. Some of them are suspected to be ''artifacts'' not removed by the Black and Hallet (1986) method. An isolated large particle creates an isolated peak in $N(D)$, which is not statistically significant with respect to the integration time. Thus, the isolated large particles were eliminated in the $N(D)$ calculation using the following criteria. If, in a 6-s integration time, a particle of diameter D_1 is recorded while $N(D) = 0$ for all diameters D such that $D_1 - 1.0$ mm $\leq D < D_1$, then $N(D_1)$ is set to zero. In other words, any diameter class corresponding to a population greater than zero and appearing after five empty diameter classes is set to zero. This elimination process modifies 15% of the original DSD data. Its effect on the results is discussed in section 4d.

Here, the microphysical measurements for rain samples that are considered correspond to $R \geq 5$ mm h^{-1} only. This is approximately consistent with conditions used to apply the GA method to ARMAR data where a PIA threshold of 1 dB was used (see section 5). Thus, the chosen samples are more representative of moderate to heavy than light rain. This procedure led us to select 126 DSDs between 1630 and 2000 UTC. The Z, K, and R derived from these $N(D)$ data were fitted by using three power–law relations of the form

$$Z = a_1 K^{b_1}, \tag{16a}$$

$$Z = a_2 R^{b_2}, \tag{16b}$$

and

$$K = a_3 R^{b_3}. \tag{16c}$$

To determine the (a_i, b_i) coefficients, we looked for the best linear fit to the data plotted in a log–log scale. The standard least squares (LS) fit between any variable pair requires minimizing the vertical distance between the data point and the fit line. This relies on the hypothesis of a dependent variable including errors to be minimized on the y axis and an independent error-free variable on the x axis. There is, however, a natural scatter in the measured $N(D)$. This implies that the derived K, R, and Z variables are also scattered and not error free. Therefore, an orthogonal LS fit was chosen since it minimizes the perpendicular distance from the data point to the fit line, thereby taking into account the variability of both variables. To avoid dependency of the results on unit scales, every fit was performed after normalizing the extreme values of each variable to the bounds of the dimensionless interval [0–1]. In all cases, the orthogonal fit line stands between the $x(y)$ and the $y(x)$ standard fit lines. It is closer to $y(x)$ [$x(y)$] if the x variable (y variable) is less scattered than the y variable (x variable). The advantage of this method, compared with standard fits, is that any relationship can be analytically inverted. This property, further discussed when analyzing the results in section 4b, is essential in the application of the radar algorithm.

b. Relationships between Z, K, and R

The relations obtained from the microphysical analysis are displayed in Fig. 5. In Figs. 5a and 5b, the data points extend up to nearly 50 dBZ with $Z > 40$ dBZ for 25% of the points, confirming that the rain relations are mostly relevant to convective rain. The relationships obtained using the orthogonal LS fit are

$$Z = 2.24 \times 10^4 K^{1.375}, \qquad \rho = 0.97, \tag{17a}$$

$$Z = 94.7 R^{1.593}, \qquad \rho = 0.91, \tag{17b}$$

and

$$K = 0.0182 R^{1.171}, \qquad \rho = 0.98, \tag{17c}$$

where ρ is the computed linear correlation coefficient. The correlation between the variables is generally good. The most scattered results are those found for Z–R (Fig.

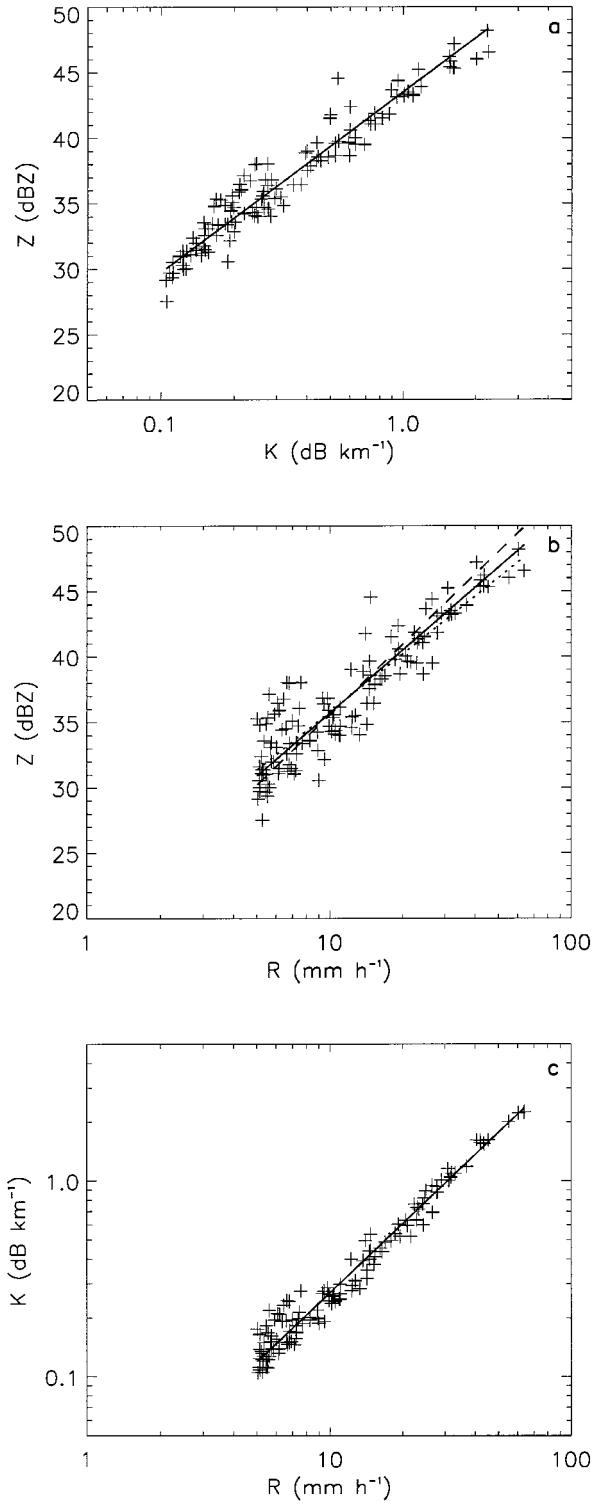

FIG. 5. Scatterplot and corresponding orthogonal least squares fit (solid line) for (a) Z vs K, (b) Z vs R, and (c) K vs R. In (b), the dotted and dashed lines correspond to the standard least squares fits for Z–R and R–Z, respectively.

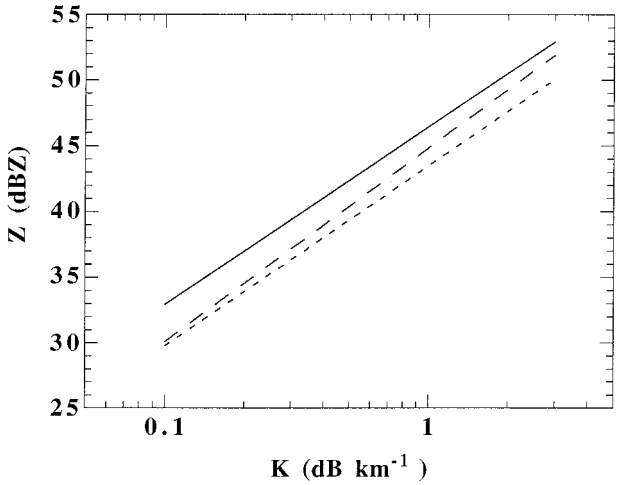

FIG. 6. The Z–K relations in a log-linear scale. The short-dashed line displays the 2DP-measured relation (17a). The solid line displays the reference-MP relation (18a). The long-dashed line displays relation (19a), which corresponds to the data fit using the original DSDs without elimination of ''marginal'' large size particles.

5b). In the following, the set of relations (17) will be referred to as the *2DP-measured* relations. Note that, owing to direct computation of Z, K, and R, from (13), (14), and (15), respectively, the 2DP-measured relations do not imply any assumption on the shape of the DSDs.

To point out the interest in using the orthogonal fit, the two standard LS fits for Z–R and R–Z are also displayed in Fig. 5b. The three fits yield notably different results. For instance, the maximum value recorded for R (64 mm h^{-1}) corresponds to 47.6 dBZ for the Z–R fit, 49.9 dBZ for the R–Z fit, and 48.5 dBZ for the orthogonal fit. Although the ''standard'' LS fit is generally used in many studies aimed at determining rain relations, in particular the Z–R relationship, the orthogonal LS fit appears to be more appropriate since it takes into account the natural scatter of the two involved variables.

Using the same computing method as for (17) described in section 4a [i.e., using Eqs. (13)–(15)], the rain relations for an exponentially shaped distribution with $N_0 = 8 \times 10^6$ m^{-4} (Marshall and Palmer 1948) were also determined:

$$Z = 4.43 \times 10^4 K^{1.356}, \tag{18a}$$

$$Z = 265.5R^{1.614}, \tag{18b}$$

and

$$K = 0.0230R^{1.190}. \tag{18c}$$

In the following, relations (18) are referred to as the *reference-MP* relations. The b_i coefficients of the reference-MP relations are very close to those of the 2DP-measured relations (17), but the a_i coefficients are different. There is a difference by a factor of about 2 in the Z–K relationships, as shown in Fig 6. This means that, for the same reflectivity, the observed DSDs provide an attenuation coefficient K nearly twice greater

than that of the reference-MP distribution. This is most likely related to the characteristics of the measured DSDs, which contain a relative number of small and medium size particles that are greater than the number of large size particles when compared with an MP distribution. Tokay and Short (1996) found similar characteristics for DSDs measured in convective precipitation during TOGA COARE using surface disdrometer measurements at Kapingamarangi Atoll (~1.00°N, 154.8°E).

c. Effect of large size particles

Large size particles are dominant in the calculation of the integral parameters. The effect of the procedure used to eliminate ''marginal'' large particles is pointed out by computing the relations from the same method but with the original DSD data including all recorded particles (real and ''artifacts''). This yields

$$Z = 3.05 \times 10^4 K^{1.476}, \qquad \rho = 0.89, \qquad (19a)$$

$$Z = 96.6R^{1.683}, \qquad \rho = 0.80, \qquad (19b)$$

and

$$K = 0.0194R^{1.157}, \qquad \rho = 0.98. \qquad (19c)$$

The K–R relations (17c) and (19c) are close to each other. This is due to the fact that R and K are moments of the distribution with close orders: approximately 3.5 for R while using the formulation of Spilhaus (1948) for the fall speed, and approximately 4 for K at 13.8 GHz following Atlas and Ulbrich (1974). More differences are found for the Z–R and Z–K relations. For instance, the maximum recorded value of K (2.26 dB km^{-1}) corresponds to 48.4 dBZ with (17a) and 50.1 dBZ with (19a). The reflectivity factor Z involved in these last two relations is more dependent than R or K on the concentration of large particles. This yields lower linear correlation coefficient and more scattered data for (19a) and (19b) than for (17a) and (17b), respectively, as illustrated in Fig. 7. Figure 6 displays relation (19a) with relations (17a) and (18a). For small values of K and Z, there are no noticeable changes due to the elimination procedure. For larger values of K and Z, relation (19a) becomes closer to the reference-MP relation (18a) than to the 2DP-measured one (17a). Thus, eliminating marginal large particles in the computation of the rain relations is important since it notably modifies the results.

d. Effect of the sampling altitude

To perform comparison with the radar results, it was assumed that the microphysical data gathered at 3.2-km altitude are representative of the whole rain layer (between sea level and 4.0-km altitude). To evaluate the altitude dependence on the rain relations, the present results are compared with those obtained at ground level at Kapingamarangi Atoll by Tokay and Short (1996).

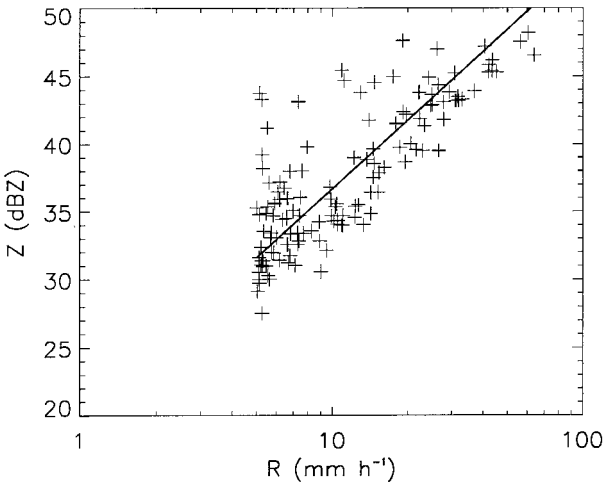

FIG. 7. Scatterplot of Z vs R and corresponding orthogonal least squares fit (solid line) for the original DSDs without elimination of marginal large size particles.

Using disdrometer measurements recorded during the experiment (November 1992 to February 1993), they found for convective precipitation with a standard LS fit:

$$Z_R = 139R^{1.43}, \qquad (20a)$$

where Z_R is the reflectivity factor calculated while using the Rayleigh approximation. In the same conditions, the 126 DSDs selected in this study lead to

$$Z_R = 135R^{1.39}, \qquad (20b)$$

while the relation computed assuming the MP case (exponential DSD with $N_0 = 8 \times 10^6$ m^{-4}) yields

$$Z_R = 308R^{1.59}. \qquad (20c)$$

Relations (20a) and (20b) are close to each other, but both are very different from relation (20c). Relation (20b) provides values of Z (dBZ) approximately 2% smaller than relation (20a) for a 5–100 mm h^{-1} R range. This difference may be caused by 1) the evolution of the DSD characteristics with altitude, 2) the number of samples that is much greater in the disdrometer case than in the airborne case, and 3) the different fall speed–diameter relationship (Beard 1976) used to get (20a). Also, relation (20b) obtained from samples with $R \geq 5$ mm h^{-1} may include some contribution from stratiform rain while the Tokay and Short (1996) result in (20a) refers to convective rain only. Nevertheless, the relations obtained at ground level and at 3.2-km altitude are still comparable, indicating that the Z–R relation does not seem to change much within the rain layer. Thus, it can be considered that the 2DP-measured relations are rather well representative of the entire rain layer when further comparing them with results of the GA method.

TABLE 1. *Z–K* relations obtained from the study of various effects referred to in column 1 and corresponding correlation coefficient ρ.

Tested effect	*Z–K* relation	ρ
Small size particles	$Z = 2.24 \times 10^4 K^{1.377}$	0.97
Incidence angle	$Z = 2.22 \times 10^4 K^{1.373}$	0.97
Drop temperature (15°C)	$Z = 2.20 \times 10^4 K^{1.351}$	0.97
Drop temperature (5°C)	$Z = 2.29 \times 10^4 K^{1.400}$	0.96

e. Other effects

Other points that had to be examined are the possible effects on the relations of the small size particles, the incidence angle, and the drop temperature.

To test if a high concentration of smaller size particles could significantly contribute to the integral parameters, the 2DC probe data involving particles between 25 and 200 μm were also used. The *Z–K* relation obtained by combining the 2DC and 2DP data, instead of the 2DP data only, is given in Table 1. The coefficients of this relation differ from (17) by less than 0.5%.

A nadir looking was chosen to determine the backscattering and extinction cross sections used in the calculation of *Z* and *K*, respectively. The radar measurements are made at incidence angles varying between 0° (nadir) and 18° (off nadir). The *Z–K* relation obtained from the microphysical data assuming an incidence angle of 18° is given in Table 1. It is very close to the 2DP-measured relation (17a) with less than 1% difference in the coefficients.

A mean drop temperature of 10°C was assumed in the rain layer to establish the 2DP-measured relations. Estimating that uncertainty in raindrop temperature is approximately ±5°C, the *Z–K* relations were also computed for 15°C and 5°C drop temperatures (see Table 1). Both relations point out a maximum difference in *Z* of 0.2 dB for *K* ranging between 0.1 and 3 dB km^{-1}.

Sensitivity results given in Table 1 show that the effects on the *Z–K* relation of the small size particles, the incidence angle, and the drop temperature are negligible. It was verified that these effects are also very small for the *Z–R* and *K–R* relations.

f. Selected relations for comparison with radar results

As explained in section 3, the GA method requires the use of a consistent set of three rain relations in which each relation can be derived from the analytical combination of the other two. Such a combination using standard LS fits depends on the chosen relations. For instance, to calculate the *Z–R* relation, *Z*(*K*) or *K*(*Z*) can be combined with either *K*(*R*) or *R*(*K*). This problem does not appear when using the orthogonal fit since each relation can be inverted analytically. Thus, there is only one way to combine two relationships. The remaining problem is to decide which relation has to be recalculated from the other two to get a consistent set. Since the 2DP-measured *Z–R* relation is the more scattered one, we choose to recalculate the *Z–R* relation from the combination of the 2DP-measured *Z–K* relation (17a) and *K–R* relation (17c), yielding

$$Z = 91.0R^{1.609}. \tag{21}$$

Relation (21) is very close to relation (17b) with a difference in *Z* of 0.06 dB for $R = 5$ mm h^{-1}, and of 0.15 dB for $R = 100$ mm h^{-1}. This is likely related to the fact that the orthogonal fit takes into account the scatter of the two variables in all relations. The set of relations (17a), (17c), and (21), hereafter referred to as the *2DP-derived* relations, will be used in the comparison with the radar results. Similarly to the 2DP-measured relations, the 2DP-derived relations are not attached to a specific shape of the DSDs.

g. Mean characteristics of the DSDs

It is useful to examine to what extent assuming constant N_0 for the DSDs in the GA method is a valid assumption, and what is the corresponding N_0 value if it exists. For this purpose, RAIN Parameter Diagrams (RAINPADs) of the sort proposed by Ulbrich and Atlas (1978) are used. Figure 8 shows the 2DP-derived relation (17a) in a *Z–K* RAINPAD constructed for an exponential distribution ($\mu = 0$), and shows isopleths of D_0, N_0, and *R*. The *Z*, *K*, and *R* values are calculated using (13), (14), and (15), respectively. The 2DP-derived *Z–K* relation corresponds to the isopleth $N_0 \approx 5 \times 10^7$ m^{-4}. The 2DP-derived *Z–R* and *K–R* relations plotted in *Z–R* and *K–R* RAINPADs (not shown here), respectively, provide the same constant N_0 value. Moreover, the N_0 obtained from the RAINPAD is very close to the mean N_{0m} ($= 5.3 \times 10^7$ m^{-4}) obtained directly from averaging N_0 values derived for each DSD (by using the fourth- and sixth-order moments).

Comparison between the sets of relations (17) and (18) shows that the b_i exponents obtained from the microphysical measurements are very close to those found for exponential DSDs with constant N_0. In fact, the b_i values depend on the μ parameter while assuming Γ-shaped DSDs and choosing b_i values is equivalent to prescribe the shape of the distribution. In the present case, an exponential shape model with constant N_0 provides results consistent with the microphysical measurements. A possible explanation for this may be that the DSD samples used for deriving the rain relations are representative for ''mean'' conditions covering a large spatial extent and a long time interval in the rain system during the aircraft flight.

5. Analysis of radar results and discussion

To apply the GA method and to determine the bulk correction factor f_B for every rain sequence *S*1 and *S*2, three *N* sets of paths were selected corresponding to beam incidence $\theta = 0°$(nadir), 10°(off nadir, cumulating

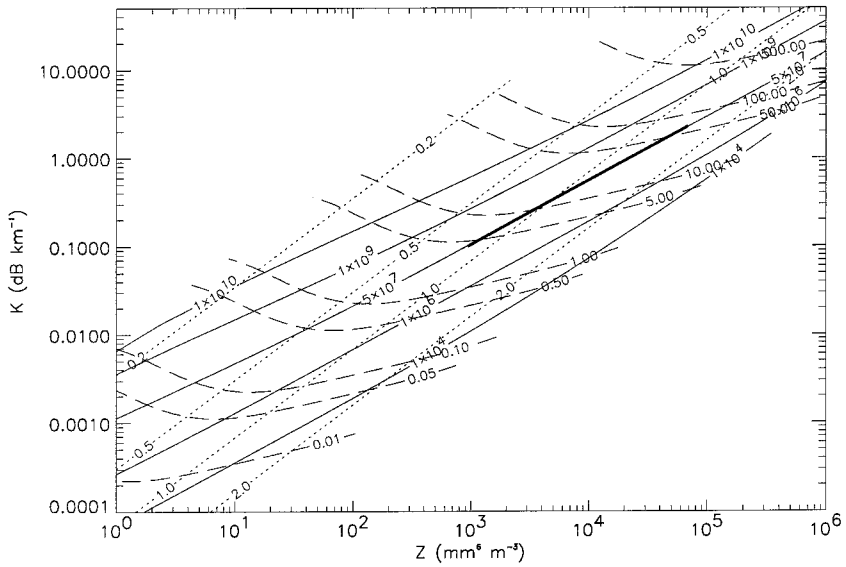

FIG. 8. Rain parameter diagram of K vs Z for an exponential DSD with the associated isopleths of N_0 (m^{-4}; solid lines), D_0 (mm; dotted lines), and R (mm h^{-1}; dashed lines). The bold line corresponds to the 2DP-derived Z–K relation (17a) over the measured rain-rate range.

left and right azimuths), and 18°(off nadir, cumulating left and right azimuths), respectively. In each case, only paths for which the rain top was above 5-km altitude and the PIA greater than 1 dB (i.e., a value slightly above the typical rms error in σ^0 estimate outside rain) were selected for the fit. The rain top was taken at range r_0 of the first detectable signal along the path. Since precipitation is assumed to be rain everywhere along every path, attenuation effects may be somewhat underestimated in a well-identified melting region and overestimated in an ice region above the melting zone in stratiform precipitation. However, such regions have either a small range extent (in the former case) or correspond to low reflectivity (in the latter case) and weakly contribute to the total PIA.

As in case 1 the reference-MP relations (18), which correspond to an exponential DSD with $N_0 = 8 \times 10^6$ m^{-4}, are used. Results given by the GA method for the correction factor f_B are given in Table 2. The number of paths N, the rms deviation, and the linear correlation coefficient ρ of every fit are also indicated. The fits are of good quality and are very stable for the three incidence angles and the two sequences. The f_B values are obtained with a typical accuracy of 5%. The mean value is $f_B = 0.51$. It was verified that results were not very sensitive to change in the β value (the fixed exponent of the used K–Z relation) or to a bulk bias in A_{tm} (the measured PIA from surface echo). Typical numbers found are as follows: a $\pm 10\%$ change in β produces a $\pm 5\%$ change in f_B, while an artificial shift of 1 dB (-1 dB) in A_{tm} modifies f_B by -8% ($+8\%$).

TABLE 2. The f_B adjustment for rain sequences S1 and S2, and for various off-nadir beam incidence angle θ using the reference-MP Z–K relation (18a) as the initial relation. Here, N is the number of paths involved in the fit, rms is the root-mean-square deviation of the fit, and ρ is the linear correlation coefficient. For off-nadir incidences, the results are obtained by accumulating measurements at both right and left azimuths from the aircraft during the cross-track scan of the radar beam.

Sequence	θ (deg)	N	rms (dB)	ρ	f_B
S1	0 (nadir)	122	0.72	0.94	0.52
S1	10	270	0.97	0.90	0.49
S1	18	253	1.43	0.76	0.55
S2	0 (nadir)	248	0.95	0.81	0.52
S2	10	513	0.95	0.79	0.49
S2	18	394	0.92	0.80	0.49

The correlation between the total PIA (expressed in decibels greater than 0) calculated from rain echoes (PIA1) and from surface echo (PIA2) obtained for sequence S2 and nadir pointing is illustrated in Fig. 9. The estimator PIA1 from rain (on the abscissa) is not the same estimator that corresponding to (3). Instead, a PIA factor estimator based on integration of path attenuation from the surface range r_s up to any range r (Amayenc et al. 1996) is used:

$$A(r_0, r_s) = [1 + \gamma(A_{tm} f_B)^{-1/\beta} S(r_0, r_s)]^{-\beta}, \quad (22)$$

when the correction factor f_B is taken into account and integration is performed up to the rain top range r_0. This estimator, which does not require additional hypothesis, is obtained by combining (3) and the total PIA factor in the rain layer estimated by A_{tm} and still involves an integration of rain echoes via the $S(r_0, r_s)$ term. It has two main advantages with respect to (3). First, it always provides a positive estimate of $A(r_0, r_s)$ even for the low attenuation case, which is not necessarily the case for (3). Second, its comparison with A_{tm} points out directly the existence of a stable correction factor, if it exists,

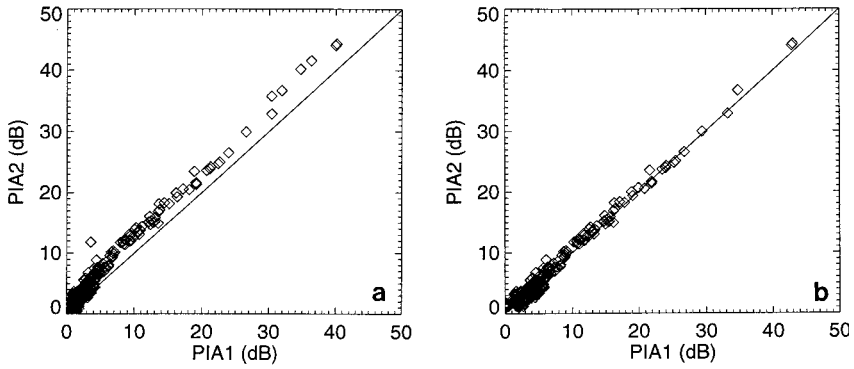

FIG. 9. Scatterplot of the total path-integrated attenuation (decibels greater than 0) PIA2 deduced from surface echo vs PIA1 deduced from rain echoes (see text), for data of sequence S2 at nadir: (a) without f_B adjustment ($f_B = 1$) and (b) with f_B adjustment ($f_B = 0.52$).

as a shift between the two PIA factor estimators, with an asymptotic limit of $A(r_0, r_s)/A_{tm} \approx f_B$ (or $10 \log f_B$ in decibels) for large PIAs. This bias is clearly seen in Fig. 9a and was obtained while assuming $f_B = 1$ in (25). Conversely, in Fig. 9b, obtained with $f_B = 0.52$ (the derived correction factor for the involved rain sequence) in (22), the bias is eliminated, and the correlation between the two PIA estimates becomes quite good. The results of Fig. 9 also show that an accurate determination of the correction factor f_B requires a large dynamic range of the involved PIA values. This confirms again that f_B is more representative of moderate to heavy rain than light rain.

Results of radar calibration procedures applied during TOGA COARE indicated a good stability of the radar constant within a 0.5-dB margin during the whole experiment, as reported in the user's guide to ARMAR TOGA COARE data (7 February 1994) provided by the experimenters of the Jet Propulsion Laboratory. Besides, the observed stable agreement (within 0.5 dB) between radar-derived σ^0 values in clear air, and model predictions or other data (Tani et al. 1995) at $\theta = 10°$, where σ^0 is known to be almost insensitive to surface wind, is also a very good indicator of a low calibration error ($\delta C \approx 1$). In these conditions, f_B may be interpreted primarily as an adjustment of α in the $Z = \alpha K^\beta$ relation, the implication of which is discussed below.

Using $f_B = 0.51$ to correct the reference-MP relation, (18a) yields the ARMAR-*adjusted Z–K* relation:

$$Z = 2.26 \times 10^4 K^{1.356}, \tag{23a}$$

which is very close to the 2DP-derived *Z–K* relation (17a) (as illustrated in Fig. 10a). Thus, the GA method appears to be able to retrieve the relation calculated from the microphysical data. As explained in section 3, the adjustment may be interpreted as a change of N_0 for N_0^*. Using $f_B = 0.51$ in (10) yields $N_0^*/N_0 = 6.63$, and the adjusted value is $N_0^* = 5.30 \times 10^7$ m^{-4} when referring to $N_0 = 8 \times 10^6$ m^{-4}. The N_0^* value is very close to that (5×10^7 m^{-4}) derived from the RAINPAD for exponential distributions (Fig. 8), and identifies to the mean N_{0m} (5.30×10^7 m^{-4}) from DSD data averaging (see section 4). Thus, there is an excellent agreement between the estimation of N_0 from the GA method and the analysis of the microphysical data, and interpreting the *Z–K* relation adjustment in terms of N_0 change is likely valid.

Then, using (11) and (12), the new *Z–R* and *K–R* relations are

$$Z = 83.1R^{1.614} \tag{23b}$$

and

$$K = 0.0161R^{1.190}. \tag{23c}$$

They are very close to the 2DP-derived relations (21) and (17c) as illustrated in Figs. 10b and 10c. This is also a consequence of the good agreement found between the adjusted N_0^* and the mean N_{0m} derived from microphysical results.

As in case 2, the 2DP-derived relations (17a,b) and (21) are used as initial relations in GA method. The results are summarized in Table 3. Similar to case 1, the results are stable with respect to the incidence angles and the time sequence. Again, the f_B values are obtained with a typical accuracy of 5%. The mean value of f_B for case 2 is 0.985, and the corresponding ARMAR-adjusted *Z–K* relation is

$$Z = 2.21 \times 10^4 K^{1.375}, \tag{24a}$$

which is very close to the initial one (17a) since f_B is nearly equal to 1. Using $f_B = 0.985$ leads to $N_0^*/N_0 = 1.04$. Then, $N_0^* = 5.2 \times 10^7$ m^{-4} when referring to the initial value $N_0 = 5 \times 10^7$ m^{-4} (from the RAINPAD). Thus, there is almost no change in N_0, and in the *Z–R* and *K–R* relations given by

$$Z = 88.8R^{1.609} \tag{24b}$$

and

$$K = 0.0181R^{1.171}. \tag{24c}$$

The similarity between the initial and the adjusted relations is also illustrated in Fig. 10.

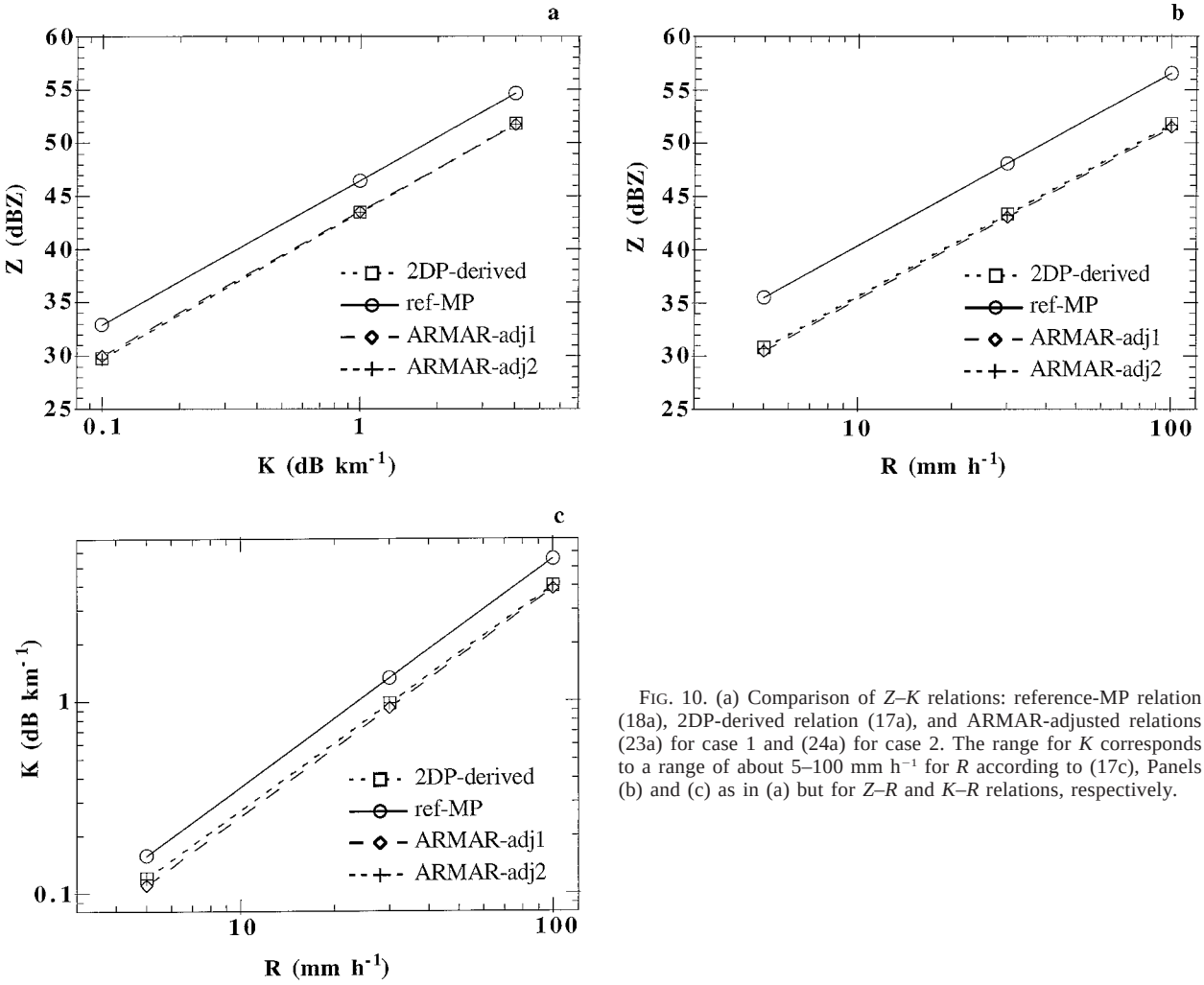

FIG. 10. (a) Comparison of *Z–K* relations: reference-MP relation (18a), 2DP-derived relation (17a), and ARMAR-adjusted relations (23a) for case 1 and (24a) for case 2. The range for *K* corresponds to a range of about 5–100 mm h^{-1} for *R* according to (17c), Panels (b) and (c) as in (a) but for *Z–R* and *K–R* relations, respectively.

The previous results have shown that the GA method is able to retrieve the ''mean'' N_0 parameter and the rain relations actually derived from microphysical data—both cases 1 and 2, which start from different initial rain relations in the radar algorithm.

In case 1, assuming exponentially shaped DSDs, the b_i exponents in the initial relations are very close to those of the 2DP-derived relations. This is why the adjustments may appear so good. However, assuming Γ-shaped distributions (with $\mu \neq 0$) in initial relations would imply exponents different from the observed ones. Thus, it is useful to check the actual results for f_B and for the adjusted relations. For this, Γ-shaped DSDs with $\mu = 2$ and $N_0 = 10^{13}\ \mathrm{m}^{-4}\ \mathrm{m}^{-\mu}$ were assumed. The value for μ corresponds to the most frequently observed one during the TOGA COARE experiment according to the results of Ulbrich (1995), who analyzed 14 556 DSD measurements from the 2DP probe aboard the Electra. The N_0 value was chosen arbitrarily to provide an initial *Z–K* relation reasonably close to the reference-MP ones. The same computation procedure as in case 2 provides a new set of initial rain relations referred to as reference-Γ relations:

$$Z = 4.36 \times 10^4 K^{1.285}, \tag{25a}$$

$$Z = 452.8R^{1.469}, \tag{25b}$$

and

$$K = 0.0286R^{1.143}. \tag{25c}$$

Then, with these new initial relations the GA method

TABLE 3. As in Table 2 but using the 2DP-derived Z–K relation (17a) as the initial relation.

Sequence	θ (deg)	N	rms (dB)	ρ	f_B
S1	0 (nadir)	122	0.71	0.94	1.03
S1	10	270	0.95	0.90	0.97
S1	18	253	1.28	0.84	0.98
S2	0 (nadir)	251	0.99	0.80	1.01
S2	10	536	1.15	0.77	0.95
S2	18	354	0.91	0.80	0.97

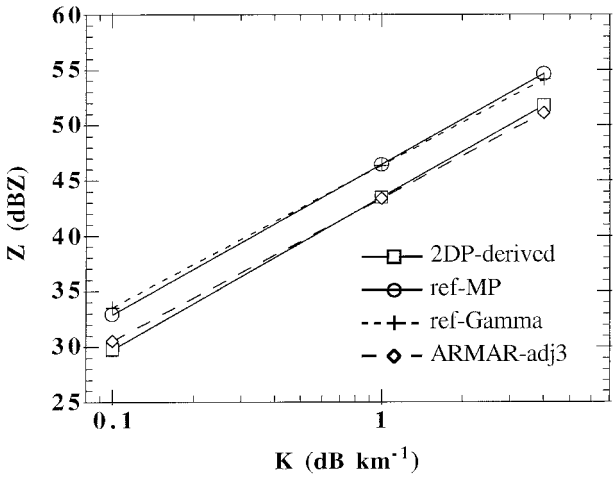

FIG. 11. Comparison of ARMAR-adjusted *Z–K* relation for case 3 and 2DP-derived *Z–K* relation. The initial reference-Γ relation and the reference-MP relation are also shown.

(case 3) provides $f_B = 0.50$ and the ARMAR-adjusted relations become

$$Z = 2.18 \times 10^4 K^{1.285}, \quad (26a)$$

$$Z = 144.7R^{1.469}, \quad (26b)$$

and

$$K = 0.0202R^{1.143}. \quad (26c)$$

The reference-Γ *Z–K* relation (25a) and the ARMAR-adjusted *Z–K* relation (26a) for case 3 are plotted in Fig. 11, along with the 2DP-derived *Z–K* relation (17a), which is unchanged. As mentioned previously, the reference-Γ relation is close to the reference-MP relation (18a), also plotted in Fig. 11, though their slopes are different. The slope of the ARMAR-adjusted relation (which is identical to that of the reference-Γ relation) differs from that of the 2DP-derived *Z–K* relation, but the adjustment still provides consistent results in the sense that the ARMAR-adjusted relation is still close to the 2DP-derived relation. The same features are obtained for the *Z–R* and *K–R* relations. It was also verified that changing N_0 to define the initial set of reference-Γ relations, though modifying the f_B value, does not rule out the previous conclusion. This indicates that the GA method results are exploitable even if the assumption of exponentially shaped DSDs is not verified.

Results of the GA method for case 1 (exponentially shaped DSDs hypothesis) are shown in Fig. 12, which displays a vertical cross section of the retrieved reflectivity factor field for the part of sequence S2 shown in Fig. 3. A comparison between Figs. 12 and 3 shows that high reflectivities are retrieved in convective rain (ray numbers 30 to 45) as expected from the large values of the PIA in this region. The peak of the raincell core is approximately 55 dBZ next to the surface. The differences are weaker for light rain in the stratiform region, for ray numbers above 60, where the PIA is low. The spike seen near ray number 70 is a consequence of the island overflight alluded to in the comments of Figs. 3 and 4 (see section 2). The results for case 2 with adjustment ($f_B = 0.985$) or without adjustment ($f_B = 1$) would be very close to those of case 1 with adjustment ($f_B = 0.51$) since they correspond to nearly identical relations (cf. Fig. 10).

Figure 13 shows scatterplots of all rain rates *R*1 in the altitude slab 250–500 m, obtained from the GA method (case 1) using the set of ARMAR-adjusted rain relations (23), with respect to rain rates *R* derived from

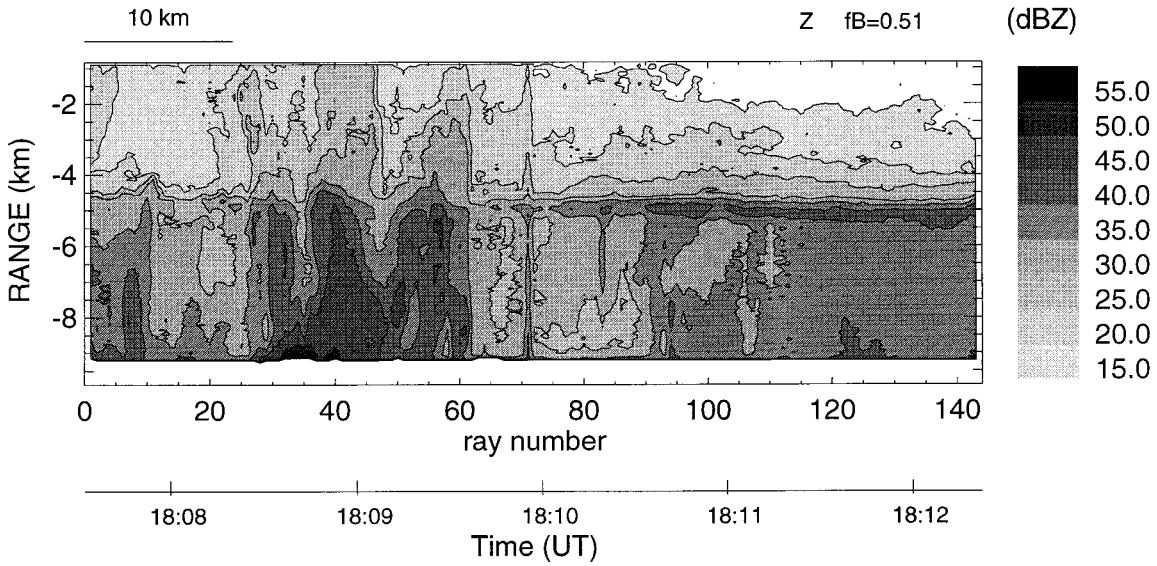

FIG. 12. As in Fig. 3 but for the reflectivity factor field retrieved from the GA method.

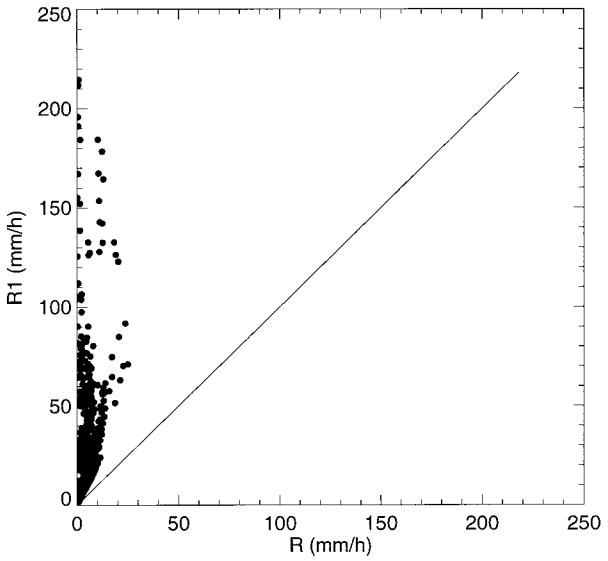

FIG. 13. Scatterplot of rain rates $R1$ retrieved from the GA method (case 1) vs rain rates R deduced from the Z–R relation (18b) using ''apparent'' Z_m values for all points within the altitude slab 250–500 m of rain sequence S2 at nadir. The solid line is the bisector.

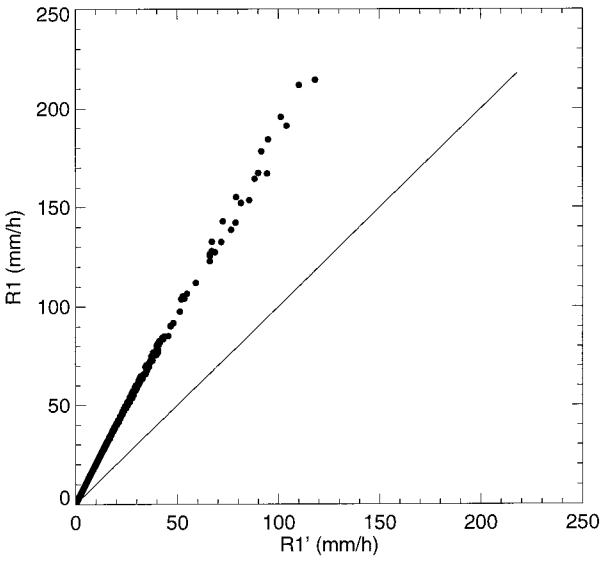

FIG. 14. As in Fig. 13 but for rain rates $R1$ from the GA method (case 1) with adjustment ($f_B = 0.51$) vs rain rates $R1'$ from the GA method without adjustment ($f_B = 1$).

the initial reference-MP Z–R relation (18b) applied to the apparent reflectivity Z_m measurements uncorrected for PIA effects. The Z_m–R estimates show a ''saturation'' effect near 10–15 mm h^{-1} while a large dynamic range of rain rates, up to more than 100 mm h^{-1} for some points within raincell cores, is recovered from the GA method. The mean rain rate over the 1515 data points is $\langle R1 \rangle = 18.9$ mm h^{-1} for the GA method and $\langle R \rangle = 3.6$ mm h^{-1} for the Z_m–R estimate.

It is useful to characterize globally the effect of the adjustment of rain relations on the rain-rate estimates. Figure 14 shows scatterplots of the rain rates $R1$ from the GA method (case 1) with respect to rain rates $R1'$ obtained without f_B adjustment [i.e., using the set of rain relations (18a, b, c), which is equivalent to using $f_B = 1$]. The mean rain rate is $\langle R1' \rangle = 9.5$ mm h^{-1} without adjustment. The relative rms deviation and bias between the two estimates are 102.8% and −99.3%, respectively. Thus, the net effect of adjusting the rain relations is to increase the rain rates by a factor of about 2.

Figure 15 displays the rain rates $R1$ from the GA method for case 1 (exponentially shaped DSDs hypothesis) with respect to rain rates $R3$ for case 3 (Γ-shaped DSD hypothesis). The two rain estimates are close to each other. The mean rain rate for case 3 is $\langle R3 \rangle = 18$ mm h^{-1}. The relative rms deviation and bias between the two estimates are 17.2% and −5.2%, respectively. Most of the observed differences occur for $R > 100$ mm h^{-1}, which correspond to raincell core centers. Thus, rain-rate estimates from the GA method are not very sensitive to the hypothesis on the DSD shape to adjust the rain relations except at very high rain rate.

Figure 16 shows a horizontal cross section at 500-m altitude of the rain-rate field retrieved from the GA method for case 1. In along-track direction (abscissa), the time frame is similar to those shown in Figs. 3 and 12. The ray numbering, however, is slightly different because larger angular intervals are used to sort the data to get similar numbers of points for every involved incidence. In the cross-track direction (ordinate), the horizontal distance is about 5 km between the indicated limits ($\pm 15°$) of the scanned incidence angles. Note that, to keep the picture easily readable, the along-track and

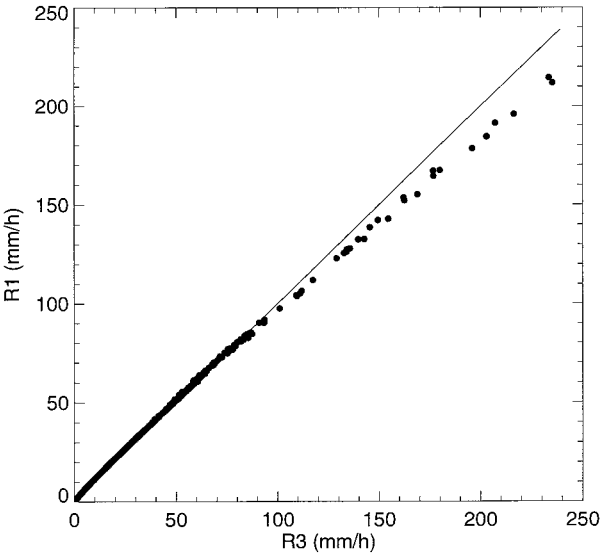

FIG. 15. As in Fig. 13 but for rain rates $R1$ from the GA method for case 1 vs rain rates $R3$ from the GA method for case 3.

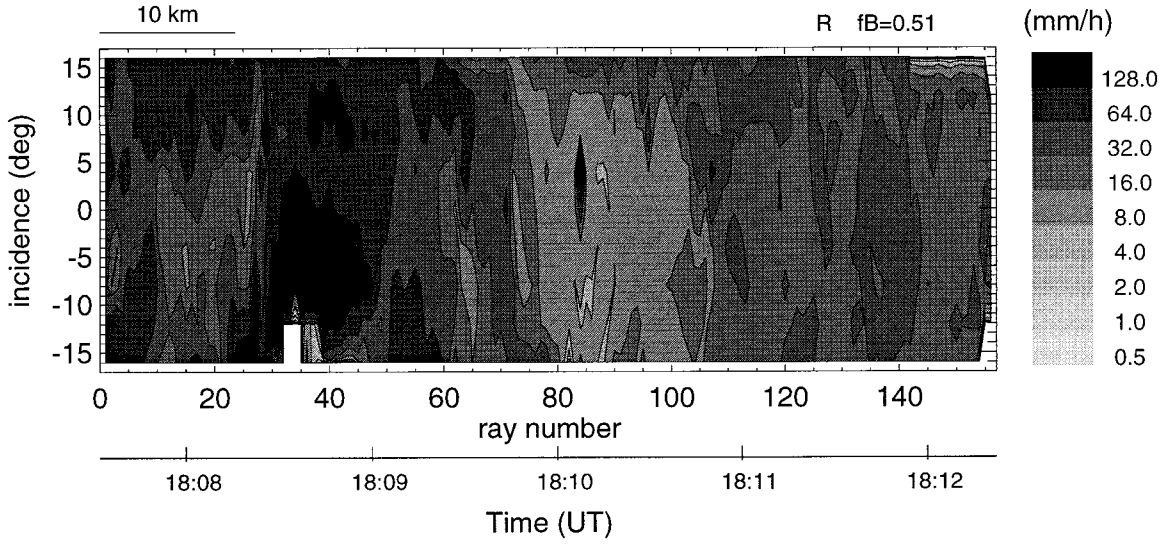

FIG. 16. Horizontal cross section of the rain-rate field recovered from the GA method for case 1, at 500-m altitude. The ordinate indicates the off-nadir incidence angle of the radar beam, from $-15°$ (left azimuth) to $+15°$ (right azimuth) in the cross-track scan. The corresponding cross-track horizontal scale is approximately 5 km. In the along-track direction, the picture is limited to the same time frame as in Figs. 3 and 12. Ray numbers refer to nadir paths. The equivalent along-track scale is indicated in the upper left of the panel.

cross-track horizontal scales are different. The maximum rain rate, in excess of 100 mm h^{-1}, is observed near ray number 40 and $-5°$ incidence, which corresponds to the center of a raincell core. The right part of the figure points out lower rain rates obtained in the more stratiform rain region with, however, local patches of rain in excess of 20 mm h^{-1}. The sharp isolated rain peak, seen near ray number 84 (instead of 70) and incidence $+5°$, is a spurious result due to the presence of a small island alluded to earlier while commenting on Figs. 3, 4, and 12.

It is not possible to validate directly the retrieved rain rates because rain measurements at surface level did not exist over the ocean. A detailed analysis of the GA method results indicates that, near the surface, the recovered rain rates in convective areas may reach 100 mm h^{-1} and more. The recovered rain rates in excess of 100 mm h^{-1} correspond to paths through two intense rain cores near 1805:45 UTC in the first part of sequence S2 (not shown in the cross section of Figs. 3 and 13), where the total PIA peak is 45 dB, and near 1808:40 UTC in the second part of S2 where the measured total PIA peak is 33 dB. Such very high rain-rate values result from the correction for large attenuation effects. In stratiform regions, the recovered rain rates typically range from 5 to 20 mm h^{-1}. The latter value seems higher than expected for a stratiform precipitation. This may be a consequence of using a set of rain relations that is thought of being better representative of convective rain than stratiform rain. In fact, it was found that the rain relations obtained from the measured DSDs for $1 < R < 10$ mm h^{-1} were different from those used in the study, which correspond to $R \geq 5$ mm h^{-1}. Tokay and Short (1996) also found different relations in stratiform and in convective precipitation. They show that this is related to the observed DSDs, which, for the same rain rate, contain more particles of larger sizes in stratiform rain than in convective rain. One way to overcome this problem is to try a separate f_B adjustment for stratiform precipitation. Unfortunately, it was not possible to get stable f_B adjustments and reliable results when applying the GA method to selected sets of paths involving low attenuation cases only (PIA $<$ 5 dB), which can crudely be representative of stratiform rain. This clearly appears as an intrinsic limit of the GA method.

6. Conclusions

In the first part of the paper, we derived relations at 13.8 GHz among *K*, *Z*, and *R* using DSDs from airborne microphysical measurements within a rain event observed during TOGA COARE. These 2DP-derived relations are representative of moderate to heavy precipitation. They were determined using the orthogonal linear fit that appears more appropriate than the standard LS fit to account for the natural scatter of all variables. Tests have shown that cloud droplets contributed negligibly to the integral parameters and that the marginal very large particles should be eliminated since their detection is not statistically significant but notably modify the results. An important result is that attenuation effects are greater by a factor of 2 for the 5–100 mm h^{-1} rain-rate range than those predicted with relations derived from MP DSDs. This is related to the number of small particles, which is, for the same rain rate, larger in the measured distributions than in the MP distributions.

This is consistent with Tokay and Short (1996). Another important result is that the relations obtained from the airborne microphysical data appear to be very close to those obtained for exponential DSDs with constant value of $N_0 = 5 \times 10^7$ m^{-4}. The exponential shape model with constant N_0 appears to be the best model for the integral parameters considered here.

In the second part of the paper, the measured relations were compared to the relations adjusted using the GA method applied to ARMAR radar data (13.8 GHz). This method provides primarily a bulk correction factor for the α coefficient of the initial $Z = \alpha K^\beta$ relation while β is assumed to be constant. Then, assuming that the DSDs are exponentially or Γ-shaped with a constant N_0 value, correction factors for the initial N_0 value and then for the *Z–R* and *K–R* relations may be inferred. Comparison between the relations derived from the microphysical measurements and from the GA method was performed using three different sets of initial relations in the GA method. Case 1 corresponds to an MP exponential distribution with $N_0 = 8 \times 10^6\ m^{-4}$. In this case, the algorithm is able to retrieve first a *Z–K* relation, then the constant N_0 value and *Z–R* and *K–R* relations very close to those derived from the microphysical data analysis. For case 2, where the initial relations are the 2DP-derived ones, nearly no correction is found by the algorithm. Thus, the GA method provides reliable results for both cases 1 and 2 where an exponential form for the distribution is assumed. Case 3 aims at testing the impact of the assumption concerning the distribution shape (or value of the β coefficient) using a gamma distribution with constant N_0 and $\mu = 2$. The algorithm provides, in this case, relations as close as possible to the 2DP-derived ones. The effect of the GA method on the retrieved rain rates was found to be nearly similar for the three cases. This work shows that the GA method is a reliable range-profiling algorithm for the studied rain system, although it appears more appropriate for convective than for stratiform precipitation.

Acknowledgments. The authors would like to thank the Process Studies Program Office (code SEP, NASA Headquarters) and the Distributed Active Archive Center (code 902.2) at Goddard Space Flight Center, Greenbelt, Maryland, for the production and distribution of these data respectively. The authors express their appreciation to F. Marks, P. Willis, and R. Black from NOAA/AOML (Miami) for providing us with the experimental drop size spectra used in this study. We also acknowledge Frank Roux, from Laboratoire d'Aérologie (Toulouse, France) for providing us with the radar reflectivity composites used in Figs. 1 and 2. Acknowledgments extend to the four anonymous reviewers for their constructive remarks.

REFERENCES

Amayenc, P., and T. Tani, 1995: Tests of algorithms for range-profiling of the rain rate from ARMAR data in TOGA-COARE. Preprints, *27th Conf. on Radar Meteorology*, Vail, CO, Amer. Meteor. Soc., 789–791.

——, J. P. Diguet, M. Marzoug, and T. Tani, 1996: A class of single- and dual-frequency algorithms for rain-rate profiling from a spaceborne radar. Part II: Tests from airborne radar measurements, *J. Atmos. Oceanic Technol.,* **13,** 142–164.

Atlas, D., 1994: Footprints of storms on the sea: A view from spaceborne synthetic aperture radar. *J. Geophys. Res.,* **99** (C4), 7961–7969.

——, and C. W. Ulbrich, 1974: The physical basis for attenuation-rainfall relationships and the measurement of rainfall parameters by combined attenuation and radar methods. *J. Rech. Atmos.,* **8,** 275–298.

Battan, L., 1973: *Radar Observation of the Atmosphere.* University of Chicago Press, 323 pp.

Beard, K. V., 1976: Terminal velocity and shape of cloud and precipitation drops aloft. *J. Atmos. Sci.,* **33,** 851–864.

Black, R. A., and J. Hallet, 1986: Observations of the distribution of ice in hurricanes. *J. Atmos. Sci.,* **43,** 802–822.

Durden, S. L., E. Im, K. Li, W. Ricketts, A. Tannier, and W. Wilson, 1994: ARMAR: An airborne rain-mapping radar. *J. Atmos. Oceanic Technol.,* **11,** 727–737.

Gunn, R., and G. D. Kinzer, 1949: The terminal velocity of fall for water drops in stagnant air. *J. Meteor.,* **6,** 243–248.

Hitschfeld, W., and J. Bordan, 1954: Errors inherent in the radar measurement of rainfall at attenuating wavelengths. *J. Meteor.,* **11,** 58–67.

Iguchi, T., and R. Meneghini, 1994: Intercomparison of single-frequency methods for retrieving a vertical rain profile from airborne or spaceborne radar data. *J. Atmos. Oceanic Technol.,* **11,** 1507–1516.

Kozu, T., and J. Nakamura, 1991: Rainfall parameter estimation from radar measurements combining reflectivity profile and path-integrated attenuation. *J. Atmos. Oceanic Technol.,* **8,** 259–270.

——, ——, R. Meneghini, and W. C. Boncyck, 1991: Dual-parameter rainfall measurement from space: A test result from aircraft experiment. *IEEE Trans. Geosci. Remote Sens.,* **29,** 690–703.

Marshall, J. S., and W. M. K. Palmer, 1948: The distribution of raindrops with size. *J. Meteor.,* **5,** 165–166.

Marzoug, M., and P. Amayenc, 1994: A class of single- and dual-frequency algorithms for rain-rate profiling from a spaceborne radar. Part I: Principle and tests from numerical simulations. *J. Atmos. Oceanic Technol.,* **11,** 1480–1506.

Meneghini, R., J. Eckerman, and D. Atlas, 1983: Determination of rain rate from a spaceborne radar using measurements of total attenuation. *IEEE Trans. Geosci. Remote Sens.,* **21,** 34–83.

——, and K. Nakamura, 1990: Range profiling of the rain rate by an airborne weather radar. *Remote Sens. Environ.,* **31,** 193–20.

——, ——, C. W. Ulbrich, and D. Atlas, 1989: Experimental tests of methods for the measurement of rainfall rate using an airborne dual-wavelength radar. *J. Atmos. Oceanic Technol.,* **6,** 637–651.

——, T. Kozu, H. Kumagai, and W. C. Boncyck, 1992: A study of rain estimation methods from space using dual-wavelength radar measurements at near-nadir incidence over ocean. *J. Atmos. Oceanic Technol.,* **9,** 364–382.

Moore, R. K., Y. S. Yu, A. K. Fung, D. Kanedo, G. J. Dome, and R. E. Werp, 1979: Preliminary study of rain effects on radar scattering from water surface. *IEEE J. Oceanic Eng.,* **4,** 31–32.

Ray, P. S., 1972: Broadband complex refractive indices of ice and water. *Appl. Opt.,* **11,** 1836–1844.

Roux, F., and M. P. Moine, 1996: Heat and momentum fluxes associated with mesoscale convective systems observed during TOGA-COARE. Preprints, *Seventh Conf. on Mesoscale Processes,* Reading, United Kingdom, Amer. Meteor. Soc., 298–300.

Simpson, J., R. F. Adler, and G. R. North, 1988: A proposed tropical rainfall measuring mission (TRMM) satellite. *Bull. Amer. Meteor. Soc.,* **69,** 278–295.

Spilhaus, A. F., 1948: Raindrop-size, shape and falling speed. *J. Meteor.,* **5,** 108–110.

Tani, T., P. Amayenc, and M. Ali-Mehenni, 1995: Radar return from the ocean surface and path-integrated attenuation at 13.8 GHz as derived from ARMAR data in TOGA-COARE. Preprints, *27th Conf. on Radar Meteorology,* Vail, CO, Amer. Meteor. Soc., 694–696.

Tokay, A., and D. A. Short, 1996: Evidence from tropical raindrop spectra of the origin of rain from stratiform versus convective clouds. *J. Appl. Meteor.,* **35,** 355–371.

Ulbrich, C. W., 1983: Natural variations in the analytical form of the raindrop size distribution. *J. Climate Appl. Meteor.,* **22,** 1204–1215.

——, 1995: Generalized rain parameter relations applied to TOGA COARE data. Preprints, *27th Conf. on Radar Meteorology,* Vail, CO, Amer. Meteor. Soc., 687–689.

——, and D. Atlas, 1978: The rain parameter diagram: Methods and applications. *J. Geophys. Res.,* **83,** 1319–1325.

Waterman, P. C., 1965: Matrix formulation of electromagnetic scatterings. *Proc. IEEE,* **53,** 805–812.

Webster, P. J., and R. Lukas, 1992: TOGA COARE: The Coupled Ocean–Atmosphere Response Experiment. *Bull. Amer. Meteor. Soc.,* **73,** 1377–1416.